Research Article Vol. 31, No. 6 / 13 Mar 2023 / *Optics Express* 9713

Optics EXPRESS

Highly efficient, modal phase-matched second harmonic generation in a double-layered thin film lithium niobate waveguide

HAOYANG DU,[1] XIUQUAN ZHANG,[2] LEI WANG,[1,*] AND FENG CHEN[1]

[1] *School of Physics, Shandong University, Jinan 250100, China*
[2] *Key Laboratory of Laser & Infrared System, Ministry of Education, Shandong University, Qingdao 266000, China*
[*] *leiwangsdu@sdu.edu.cn*

Abstract: In this contribution, we numerically investigate second harmonic generation in double-layered lithium niobate on the insulator platform by means of the modal phase matching. The modal dispersion of the ridge waveguides at the C waveband of optical fiber communication is calculated numerically and analyzed. Modal phase matching can be achieved by changing the geometric dimensions of the ridge waveguide. The phase-matching wavelength and conversion efficiencies versus the geometric dimensions in the modal phase-matching process are investigated. We also analyze the thermal-tuning ability of the present modal phase matching scheme. Our results show that highly efficient second harmonic generation can be realized by the modal phase matching in the double-layered thin film lithium niobate ridge waveguide.

1. Introduction

Thin film lithium niobate (TFLN) emerges as a promising photonics integration circuits (PIC) platform for optical communication, sensing, and metrology applications due to the excellent second order nonlinear properties of the lithium niobate core layer [1–6]. In addition, the large refractive index contrast (0.7) between the lithium niobate core film and the SiO_2 under-buffer layer enables a very tight confinement of light hence compact mode volume in ridge waveguides and ring resonators [7–10]. During the past ten years, giant improvements of device performance have been demonstrated on TFLN platform in the fields of on-chip electro-optical modulation [11–13], nonlinear new frequency generation [14–21] and heterogeneous integration with other material platforms [22–28], etc. Lithium niobate has been investigated as an effective nonlinear optical frequency generator for almost half a century. As a ferroelectric crystal, quasi-phase-matching (QPM) has been demonstrated in lithium niobate for several decades by inversing the ferroelectric domain periodically. In 2018, Cheng etc. demonstrated periodically poled ridge waveguides in TFLN which realize a normalized conversion efficiency (NCE) at an order of $10^3\%W^{-1}cm^{-2}$ in a second harmonic generation (SHG) process [14][14]. A record-high SHG conversion efficiency up to 4600% $W^{-1}cm^{-2}$ was realized with an in-situ poling/observation setup [15][15]. Jiayang Chen and Juanjuan Lu reported the on-chip ultrahigh SHG conversions (about $10^5\%W^{-1}cm^{-2}$) in TFLN micro-ring resonators in 2020 [29,30]. These reported ultrahigh conversion efficiencies should be attributed to the excellent nonlinearity of lithium niobate, compact mode areas of the TFLN ridge waveguides and the excellent quality of the resonators. Domain engineering has strict requirement on the domain uniformity, which adds challenges for on-chip TFLN devices that require small domain periods. The electrodes used in the domain engineering will also add the designing complication and lower the integration density. An alternative method to fulfill phase matching between the fundamental frequency (FF) wave and second harmonic (SH) wave is the modal phase matching (MPM) which adopts the modal dispersion of multi-mode optical

#482572
Journal © 2023

https://doi.org/10.1364/OE.482572
Received 7 Dec 2022; revised 1 Feb 2023; accepted 2 Feb 2023; published 1 Mar 2023

waveguide [31,32]. Due to the large index contrast of the ridge waveguide in TFLN, many modes can be supported especially at the shorter wavelength, e.g., SH wavelength. By adjusting the geometric dimensions and FF wavelength, the effective refractive index (n_{eff}) of high order mode of SH wave can be equal to that of the fundamental mode of FF wave. In another word, phase matching has been realized directly. The birefringence of LN can also be considered in the MPM process. MPM on TFLN photonics platform have been reported till 2017 [33–36]. An obstacle to impede the on-chip integration of MPM devices is the poor overlap between the interacting light, e.g., the SH light and FF light in the SHG process. The reported NCE of MPM scheme is about 41%W^{-1}cm^{-2} which is too low compared to the QPM Scheme [33][33]. To tackle this challenge, semi-nonlinear waveguides consisting an marvelous LN/TiO$_2$ hybrid films structure are proposed in 2019 [37], exhibiting an theoretical NCE up to the magnitude of 10^3%W^{-1}cm^{-2} (experimental value of 650%W^{-1}cm^{-2}). A group from TsingHua University also proposed a double-layered TFLN structure which consists two LN film with antiparallel polarizations (*c*-axis) theoretically [38]. In 2021, we realized an SHG process with a NCE of 5540%W^{-1}cm^{-2} in a double-layered TFLN ridge waveguides experimentally [39]. We summarized the performances of SHG ridge TFLN devices in Table 1 of the appendix. The double-layered *x*-cut LN layers with antiparallel *c*-axis could enable a MPM between the fundamental mode of pump light and high order mode of SH light. However, the potential of the double-layered TFLN integrated platform, especially the geometric dependence to MPM process, has not yet been fully explored.

Here we report on the detailed numerical investigations about SHG process in double-layered *x*-cut TFLN platform by means of MPM scheme. The effect of geometry dimensions including thickness, width, etching depth and sidewall angle on MPM process were studied for the first time. The results show that modal phase matching SHG process with high NCE (10^3~10^4%W^{-1}cm^{-2}) performance can be achieved within a quite broad range of geometric parameters, i.e., thickness and top width. The thermal-optic effect in the ridge waveguide was also investigated indicating a temperature tuning sensitivity of 0.11 nm/°C.

2. Theories and simulation details

The SHG process in TFLN ridge waveguides can be described in the following degenerated three-wave coupling nonlinear equations.

$$\frac{dA_2}{dy} = \kappa\vartheta A_1^2 e^{i\Delta\beta y} - \frac{\alpha_2}{2}A_2 \tag{1}$$

$$\frac{dA_1}{dy} = \kappa\vartheta^* A_2 A_1^* e^{-i\Delta\beta y} - \frac{\alpha_1}{2}A_1 \tag{2}$$

where A in the equations is proportional to the amplitude of the interacting light (subscript 1 for FF wave and 2 for SH wave). $\boldsymbol{\alpha_i}$ is the damping coefficient of the electrical fields. $\boldsymbol{\kappa}$ is the coupling strength, $\boldsymbol{\Delta\beta}$ is the phase mismatch, $\boldsymbol{\vartheta}$ is the nonlinear modal overlap integral, which can be written as

$$\kappa = -i\sqrt{\frac{8\pi^2 d_{eff}^2}{N_1^2 N_2 c\varepsilon_0 \lambda_2^2}} \tag{3}$$

$$\Delta\beta = \beta_2 - 2\beta_1 = 2\pi\left(\frac{N_2}{\lambda_2} - \frac{2N_1}{\lambda_1}\right) \tag{4}$$

$$\vartheta = \iint d_{nor}(x,y)E_2(x,y)E_1^*(x,y)E_1^*(x,y)dxdy \tag{5}$$

N_i is the effective refractive indices of propagating modes of pump and SHG light (1 for pump and 2 for SH wave). $E_i(x,y)$ is the normalized mode profiles, d_{eff} is the effective nonlinear coefficient, d_{nor} is the normalized nonlinear coefficient profile. Under an assumption that the power conversion from FF wave to SH wave is small, the solution of the three-wave coupling equations at the propagation $y = L$ is as the following

$$A_1(L) = A_1(0)e^{-\alpha_1 L} \tag{6}$$

$$A_2(L) = i\kappa\vartheta A_1^2(0)e^{-\frac{\alpha_2 L}{2}}\left(\frac{e^{(\frac{\alpha_2}{2}-\alpha_1-i\Delta\beta)L}-1}{\frac{\alpha_2}{2}-\alpha_1-i\Delta\beta}\right) \tag{7}$$

If the waveguide is lossless and exact phase matching is fulfilled, the theoretical NCE is:

$$\eta = \kappa^2\vartheta^2 = \frac{8\pi^2 d_{eff}^2\vartheta^2}{N_1^2 N_2 c\varepsilon_0\lambda_2^2} \tag{8}$$

For SHG with exact phase matching, the conversion efficiency increases with the pump power and propagation length. Large κ and ϑ will lead to efficient light conversion from pump to SHG light. The superiorities of TFLN device compared to Ti-diffusion/Proton exchange (PE) waveguide are the tiny core region due to the sub-micron film thickness and large index contrast. In the present concept design stage, we will focus on the factor of $\kappa^2\vartheta^2$, which is determined by the geometric design and material itself. According to Eq. (4), the modal phase matching condition of SHG process in TFLN ridge waveguide is that:

$$N_1 = N_2 \tag{9}$$

The waveguide structure we analyzed is shown in Fig. 1 (a), consisting a LN ridge core and the surrounding air/silica cladding. The orientation of LN film is x-cut and y-propagating. In a SHG process, the quasi-transverse electric (qTE) modes of pump and SHG light (polarized

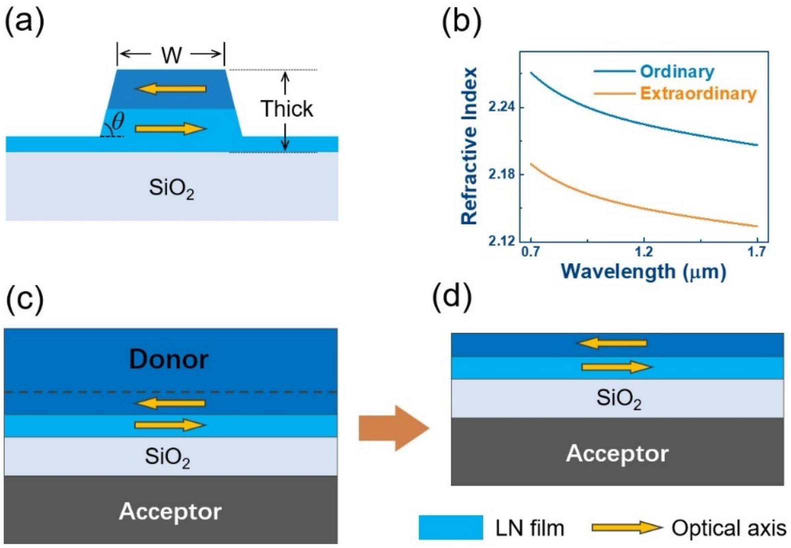

Fig. 1. (a) the Schematic of the ridge waveguide structure on double-layered TFLN. (b) the ordinary and extraordinary refractive indices of lithium niobate bulk versus wavelength. (c) One x-cut single layered TFLN acceptor is bonded to another He ion-implanted LN donor. (d) the double-layered TFLN substrate after the splitting and chemical-mechanical polishing process.

along the z-axis of the LN film) of this ridge waveguide will feel the most powerful nonlinear coefficient d_{33} (27pm/V). The silica buried oxide (SiO_2) is generally thick enough (2-4 µm) to eliminate any light leakage penetrating from the LN core to the silicon substrate. The dispersion nature of LN crystal is numerically modeled by the Sellmeier equation [40,41] showing in Fig. 1 (b). Figure 1 (c)-(d) is the fabrication of double-layered TFLN. The key step is bonding the two wafers with antiparallel polarizations. The final thickness of the double-layered TFLN can be adjusted from 400 nm-700 nm. The mode properties (mode profiles, effective refractive indices) of the ridge waveguide are calculated by a FDE solver in MODE Lumerical 2020a in the C band of optical communication and the corresponding SH wavelength. In the simulations of mode properties, the refractive indices of two LN layers are the same. In the calculation of NCE values, the nonlinear coefficient d_{33} of two LN layers are opposite.

3. Results and discussion

3.1. MPM points

Figure 2(a) shows the calculated effective indices of supported modes of FF (1550 nm) and SH waves (SH, 775 nm) as the LN core width increases from 800 nm to 1800nm. The thickness of the whole LN film is 600 nm. The etching depth is set to be 450 nm. According to the Eq. (9), the intersection points between FF and SH curves are the MPM points meaning that FF and generated SH waves are in phase when they travel along the ridge waveguide. Figure 2(b) and (c) show the three detailed MPM points at the width of 810.2 nm, 1379.4 nm and 1381.5 nm, respectively. If the LN film is monolithic and the d_{33} coefficient is uniform in the whole LN core region, the theoretical NCE ($\%W^{-1}cm^{-2}$) values for three widths (810.2 nm, 1379.4 nm and 1381.5 nm) calculated from Eq. (8) are about 167.2, 15.6 and 0, respectively. The tiny SHG conversions of 1379.4 nm and prohibition of 1381.5 nm are due to the mode antisymmetry respected to x and z axes. If we use the double-layered LN film, the corresponding theoretic NCE ($\%W^{-1}cm^{-2}$) values are about 1869.3, 8996.5 and 0, respectively. Apparently the MPM point of 1379.4 nm is very competitive due to its ultra-high conversion efficiency. Although the MPM point of 810.2 nm shows considerable efficiency in both monolithic and double-layered cases, its narrow width and electric fields extending to the sidewall region often bring high propagation loss. For MPM point of 1379.4 nm, its width is appropriate for EBL/Stepper photolithography. The electric fields of this mode are well confined in the LN core region. Therefore, we will focus on the MPM points of which mode profiles are in the style of point 1379.4 nm. In the region marked by the dotted circle shown in Fig. 2(a), there is a gap between $SHTE_2$ and $SHTE_3$ curves showing that mode hybridization occurs here. In the present ridge structure shown in Fig. 1(a), the mode hybridization is induced by the crystal birefringence, nonvertical sidewall and the air top-cladding [42,43]. In ridge waveguides with certain geometry conditions, $FFTE_0$ curve will pass through this gap and no interception with $SHTE_3$ curve can be found. The mode hybridization in the SH waveband is not the main purpose of this paper and we will investigate it in further work.

3.2. Geometric Dependence and Sensitivity of MPM process

The geometry of the ridge waveguide, including the width, thickness, etching depth and sidewall angle, are critical to the MPM process. In this part we will focus on the relation of geometry of ridge waveguide to the MPM performance. The width, thickness, etching depth, sidewall angle and relative thickness of double LN layers are swept to investigated the geometric dependence and sensitivity of the MPM process.

Figure 3(a) shows the calculated MPM wavelength of ridge waveguides with different widths and thicknesses when we fix the etching depth to be 450 nm. A minimum MPM wavelength of 1340 nm is found when the width and thickness are about 1800nm and 550 nm, respectively. A

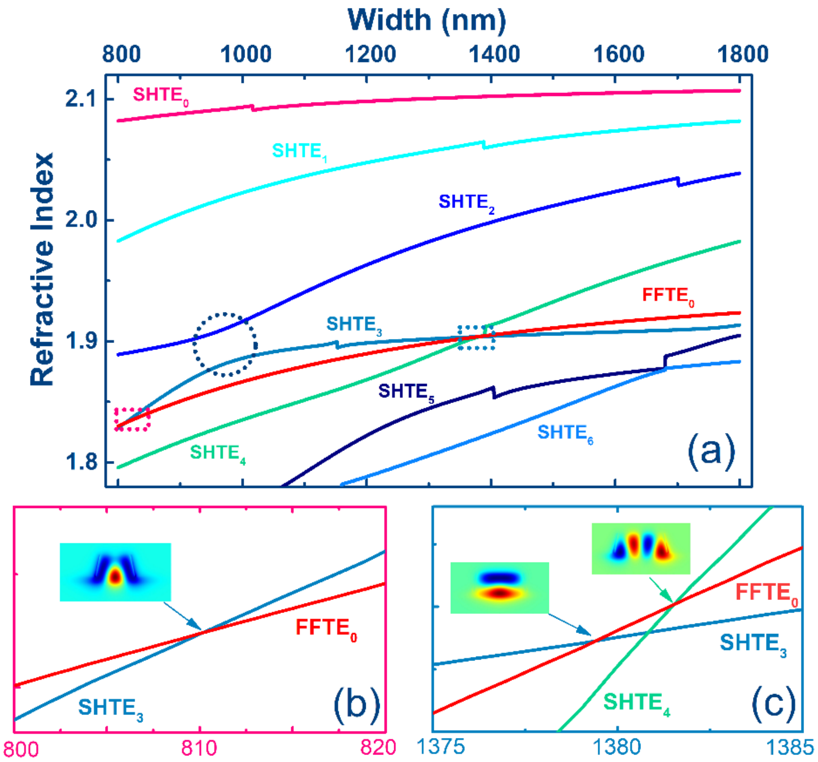

Fig. 2. (a) the effective refractive indices of FF fundamental mode and SH modes as a function of top width of ridge waveguide. (b) the MPM point at 810.2 nm; (c) the two MPM points at 1379.4 nm and 1381.5 nm. The inset figures in (b) and (c) are the electric profiles of the SH modes involved in the MPM process.

maximum of 1820nm corresponds to a ridge with width of 1000 nm and thickness of 650 nm. We depict the MPM curves of 1530 nm, 1550 nm and 1570 nm in Fig. 3(a). One can see that SHG process in the whole C band can be realized by tuning the thickness and width of the ridge waveguide in a sweet area range from thickness of 575 nm to 630 nm, which locates between the two mode hybridization regions. A such wide sweet area means large tolerance when one wants to integrate frequency converter into different positions of a whole TFLN wafer. A detailed observation about the three MPM curves reveals that thicker film corresponds to a broader width to remain the phase matching wavelength unchanged. Figure 4 indicates the calculated modal n_{eff} as a function of width, thickness and wavelength individually. Generally, the three interception points in Fig. 4 are the modal phase matching points between FFTE_0 and SHTE_3 modes. It is found from Fig. 4(a) that if the width of a ridge waveguide is broader than the phase matching width, the n_{eff} of FFTE_0 mode becomes larger than that of SHTE_3 mode. If we remain the lambda unchanged, the resulted negative $\Delta\beta$ in Eq. (4) should be compensated by a positive change of $\Delta\beta$ to maintain the phase matching condition. It is found from Fig. 4(b) that a positive increment of thickness from the phase matching point can lead to a positive $\Delta\beta$. Therefore, the negative $\Delta\beta$ induced by the broader width can be compensated by a thicker film. It is also found from Fig. 3(a) that the MPM wavelength tends to decrease when the top width of the ridge waveguide increases, while the relation between the MPM wavelength and the thickness of ridge waveguide marked a complete reversal. We can see from Fig. 4(c) that both FFTE_0 and SHTE_3 modes exhibit a normal dispersion, but the FFTE_0 mode shows a lower dispersion. As a result, the positive change of wavelength from the phase matching point could induce a negative $\Delta\beta$, which can be compensated by a narrower width and/or thicker LN film. There are two regions where the MPM wavelength shows different variation trends (marked by arrows). The discontinuities in both areas are due to the mode hybridizations appears in the SH band. Figure 3(b) shows the effective indices of MPM points versus the width and thickness of the ridge waveguides. The minimum of MPM indices is about 1.811 which is far larger than the index of buffered SiO_2 layer. The higher MPM indices for all waveguide dimensions can eliminate the leakage loss from the LN core region to the silicon/lithium niobate substrate if SiO_2 layer is thick enough, showing potential applications in the on-chip photonic integration circuits.

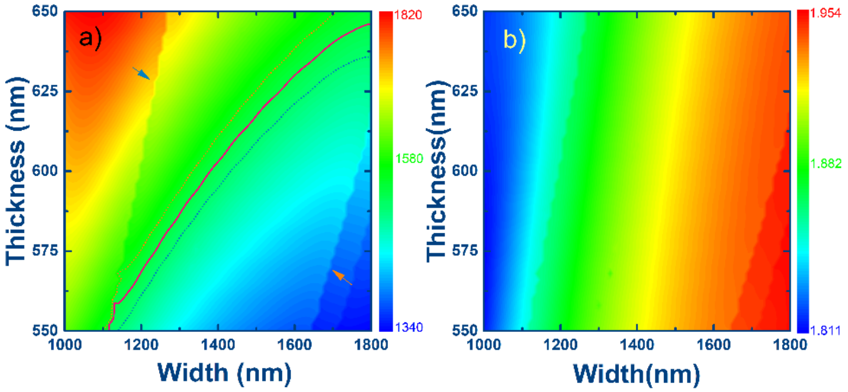

Fig. 3. (a) the phase matching wavelength as a function of thickness and top width of the ridge waveguides. Top width: 1000 nm-1800nm; thickness: 550 nm-650 nm. The contour lines of phase matching wavelength of 1530 nm, 1550 nm and 1570 nm were depicted in figure a) for a guide. (b) the effective refractive indices of MPM points as a function of thickness and top width of the ridge waveguides. In the simulations, the etching depth is set to be 450 nm.

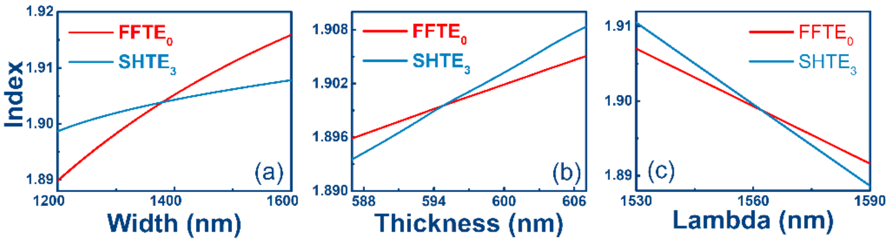

Fig. 4. (a) the effective indices of $FFTE_0$ and $SHTE_3$ modes as a function of the top width of the ridge waveguides, (b) the thickness of the ridge waveguides and (c) the wavelength. The wavelength and thickness in a) are 1550 nm and 600 nm, respectively. The width and wavelength in b) are 1350 nm and 1550 nm, respectively. The width and thickness in c) are 1350 nm and 600 nm, respectively.

Figure 5(a) shows the NCE values of MPM process versus the dimensions of width and thickness of the ridge waveguide. The thicknesses of the two LN layers are set to be the same in the calculations. The NCE values in the whole map are well above 4000%/W/cm^2. We can easily find that the maximum of NCE is realized in the ridges with smallest thickness, 550 nm, but not for the narrowest width, 1000 nm. There are two special regions of which NCE values are significantly lower than the surroundings, which have been marked by arrows. A further observation shows that the two regions coincide with the two mode hybridization regions shown in Fig. 3(a). As we know that the E_z component in the SH modes which couple with d_{33} coefficient is weak, leading to a lower NCE value near the hybridization region. It should also be noted that ridge waveguide with too compact dimensions cannot confine FF light inside LN core efficiently. This will also result weak nonlinear interaction efficiency too. The NCE values tend to be smaller when the thickness of the ridge waveguide increases. This can be explained that the mode volumes of the FFTE$_0$ and SHTE$_3$ modes become larger as the thickness of the ridge waveguide increases, leading to a less modal overlap factor in Eq. (8). Figure 5(c) depicts the NCE values of MPM and QPM as functions of the thickness of ridge waveguide along the 1550 nm curve shown in Fig. 3(a). The NCE values of MPM are larger than QPM from 575 nm to 630 nm. The maximum values of MPM and QPM are 9989 and 5924%W^{-1}cm^{-2} when the thickness is about 575 nm. The minimum values are 7154%W^{-1}cm^{-2} for MPM and 4413%W^{-1}cm^{-2} for QPM at thickness of 630 nm. The NCE values show a nearly linear relation to the thickness. One important factor determines the NCE values is the d_{eff} value involved in a SHG process. The MPM is a direct phase matching process so that the d_{eff} in a MPM process equals to d_{33}. In a QPM process, d_{33} coefficient flip over along the light propagation to ensure the constructive interference of generated SH signal in each coherent length. The maximum of d_{eff} of a QPM process in Eq. (3) is 2/π of the d_{33} coefficient. Another factor influences the conversion efficiency is the the nonlinear modal overlap integral. In Fig. 5(d) we depict the nonlinear modal overlapping integral ($\boldsymbol{\vartheta}$) along the curve of 1550 nm shown in Fig. 3(a). It is found that the overlapping values of QPM process are larger than the values of MPM from the thicknesses of 575 nm to 630 nm. For wavelength of 1550 nm, the overlapping values of QPM and MPM at the thickness of 600 nm are about 1.126 and 0.883 μm^{-1}, respectively. However, considering the overall evaluation relations in Eq. (8), the theoretical NCE values of QPM and MPM for wavelength of 1550 nm and thickness of 600 nm are about 5219% and 8737% W^{-1}cm^{-2}, respectively.

As the modal phase matching process depends on the waveguide geometrical dimensions critically, it is necessary to investigate the sensitivities of phase matching wavelength to the fluctuations of thickness, top width and sidewall angle of the ridge waveguides. Figure 6(a) shows the phase matching wavelength as a function of waveguide thickness when the top width of ridge waveguide remains stable. As we can see that the phase matching wavelength increased with the thickness of the ridge waveguides at a near-linear trend. The fitted slopes $\Delta\lambda_{\mathrm{PM}}/\Delta$Thickness as a function of widths in Fig. 6(b) shows a very high sensitivity up to 2.7 (width 1300 nm) between the phase matching wavelength and ridge thickness. Waveguide with narrow width leads to higher sensitivity of $\Delta\lambda_{\mathrm{PM}}/\Delta$Thickness.

The phase matching wavelength versus widths of the ridge waveguides are shown in Fig. 7(a) when the thickness of the ridge waveguide remains stable. Unlike the linear relations of thickness variation, a negative nonlinear trend between the width and the corresponding phase matching wavelength can be found in this figure. Figure 7(b) shows the $\Delta\lambda_{\mathrm{PM}}/\Delta$Width ratios as a function of thickness at different widths of 1300 nm, 1400 nm and 1500 nm. Waveguides with flatter cross-section show relatively lower $\Delta\lambda_{\mathrm{PM}}/\Delta$Width sensitivity. A minimum $\Delta\lambda/\Delta$Width sensitivity of 0.258 is observed in a ridge waveguide with width of 1500 nm and thickness of 580 nm. Considering the high sensitivities of $\Delta\lambda_{\mathrm{PM}}/\Delta$Thickness and $\Delta\lambda_{\mathrm{PM}}/\Delta$Width ratios, one should pay attention to the fluctuations of thickness/width along the light propagation direction, especially when a long waveguide device is preferred.

The etching depth is a critical dimension in the MPM process. Lateral leakage will happen if the etching depth is too shallow to prohibit the light coupling from the propagating mode to the orthogonally polarized slab mode. This leakage effect can be seen as a contribution to the propagation loss, which should be avoided in the design stage. Figure 8(a) shows the MPM wavelength as a function of etching depth for different film thicknesses which have been set in the simulations. The width and sidewall angle set in the simulations are 1400 nm and 75 degrees,

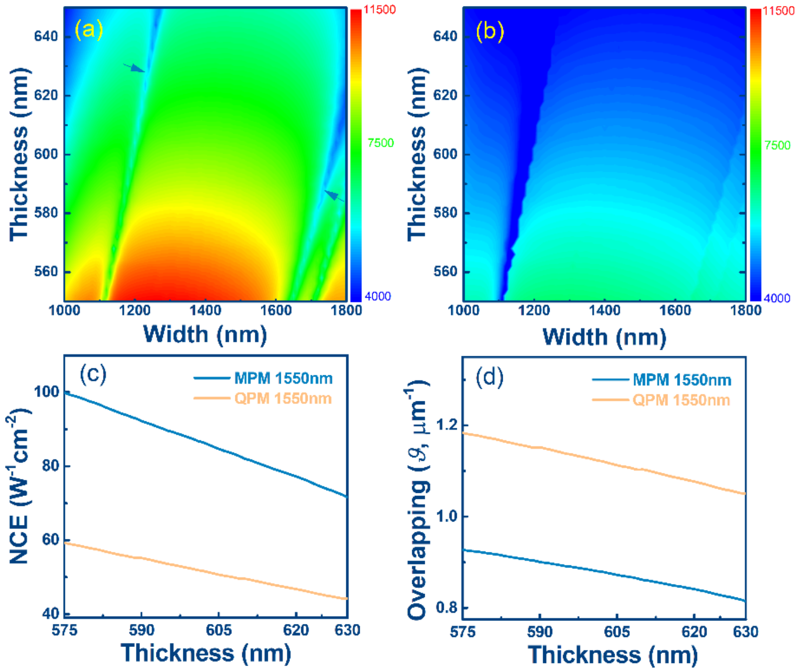

Fig. 5. (a) the normalized conversion efficiency of MPM process as a function of thickness and top width of the ridge waveguide. (b) the normalized conversion efficiency of QPM process as a function of thickness and top width of the ridge waveguide. (c) the NCE of MPM and QPM processes along the contour line of 1550 nm shown in Fig. 3(a). (d) the modal overlapping values of MPM and QPM processes along the contour line of 1550 nm shown in Fig. 3(a).

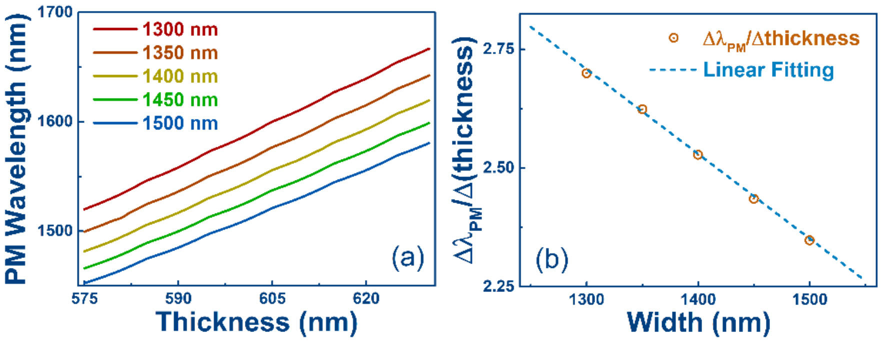

Fig. 6. (a) The phase matching wavelength versus the thickness of the ridge waveguide with different top widths and (b) the sensitivity of $\Delta\lambda_{\mathrm{PM}}/\Delta$thickness as a function of the top width of the ridge waveguide. $\Delta\lambda_{\mathrm{PM}}$ is the abbreviation of PM wavelength.

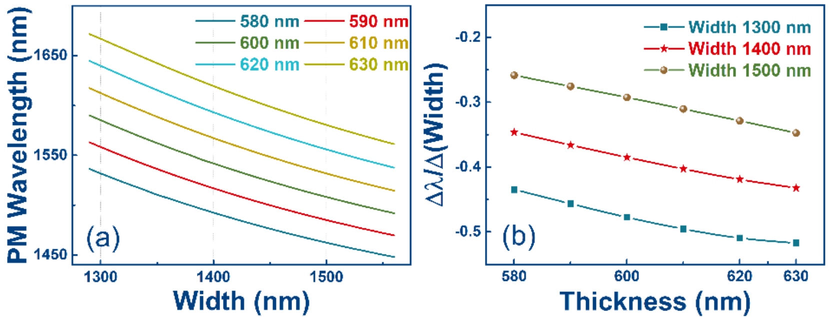

Fig. 7. (a) The phase matching wavelength versus the width of the ridge waveguide with different thicknesses and (b) the sensitivity of $\Delta\lambda_{\mathrm{PM}}/\Delta$width versus the thickness of the ridge waveguide.

respectively. The minimum of $\Delta\lambda_{\mathrm{PM}}/\Delta$depth is 0.09 for thickness of 570 nm and a maximum of 0.15 for thickness of 610 nm. The $\Delta\lambda_{\mathrm{PM}}/\Delta$depth of shallow etched TFLN ridge waveguide is 2.59 [10]. This suggests that the MPM process we studied here has a very high tolerance especially to the errors of the etching fabrications. Figure 8(b) shows the calculated NCE values versus the etching depth for different film thickness. It is found that waveguide with thinner thickness and large etching depth shows high NCE value. Deeply etched waveguide with small thickness brings a tight light confinement, hence a large nonlinear modal overlap. It can also be found in Fig. 8(a) that deep etched and thin waveguide also means short MPM wavelength. The maximum NCE value is 10410$\%$W^{-1}cm^{-2} when the thickness and etching depth are 570 nm and 500 nm, respectively.

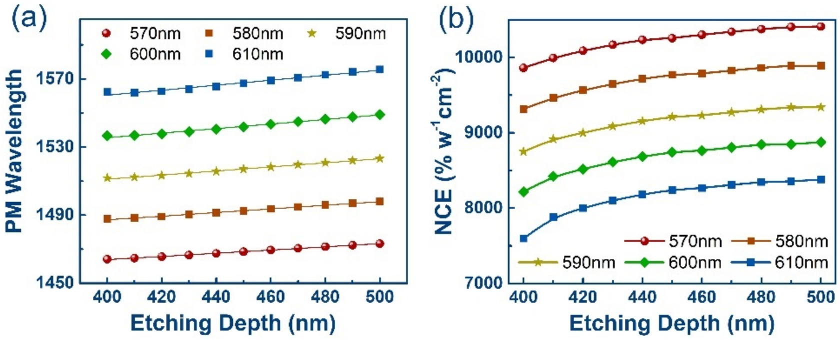

Fig. 8. (a) The phase matching wavelength versus the etching depth of the ridge waveguide with different thicknesses and (b) the NCE values as a function of the etching depth with different thicknesses.

The sidewall angle of ridge waveguides tends to be instable due to the variations of technical process and apparatus conditions. Figure 9(a) shows the phase matching wavelength as a function of sidewall angle. The top width of the ridge waveguide is set to be 1350 nm. The phase matching wavelength gets longer as the angle gets larger. When the angle is 75 degrees, the phase matching wavelength increased from 1510 nm to 1640 nm, fully covering the C + L bands of telecom. The phase matching widths versus sidewall angles are depicted in Fig. 9(b) when the phase matching wavelength is fixed to be 1550 nm. It shows a nearly linear relation between the width and sidewall angles. Linear fittings of these curves show width/angle ratios about 11 nm per degree. That means a very stringent requirement of morphological controlling in the fabrication process.

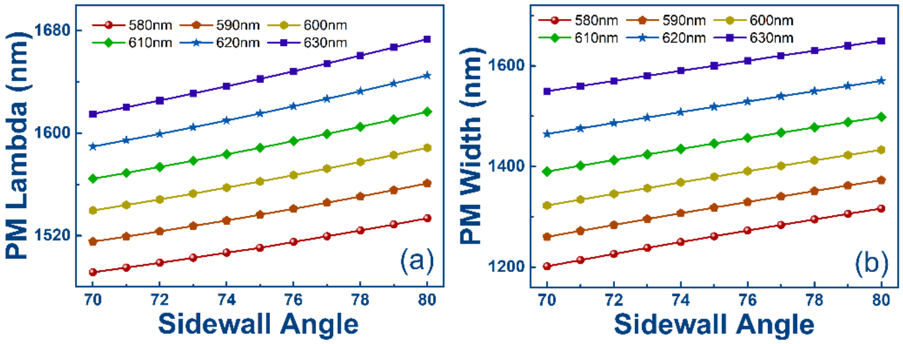

Fig. 9. (a) The phase matching wavelength versus the sidewall angle with different thicknesses. The top width is 1350 nm. (b) The phase matching width versus the sidewall angle with different thickness. The corresponding phase matching wavelength in (b) is set to be 1550 nm.

We also investigate the NCE as a function of the relative thicknesses of the double LN layers. We choose several combinations of thickness/width to maintain the MPM wavelength to be 1550 nm. Figure 10 shows the calculated NCE values as a function of the thickness of the top LN layer. It is found that the NCE curves reach its maximum around the point where the thickness of the top LN layer is one half of the total thickness, and then go down to nearly zero till the thickness of top layer equal to the total one. We also found that the maximum of each NCE curves decreases with the total thickness of the ridge waveguide due to the fact that large thickness should accompany wide width to maintain the MPM wavelength unchanged (see Fig. 3(a)).

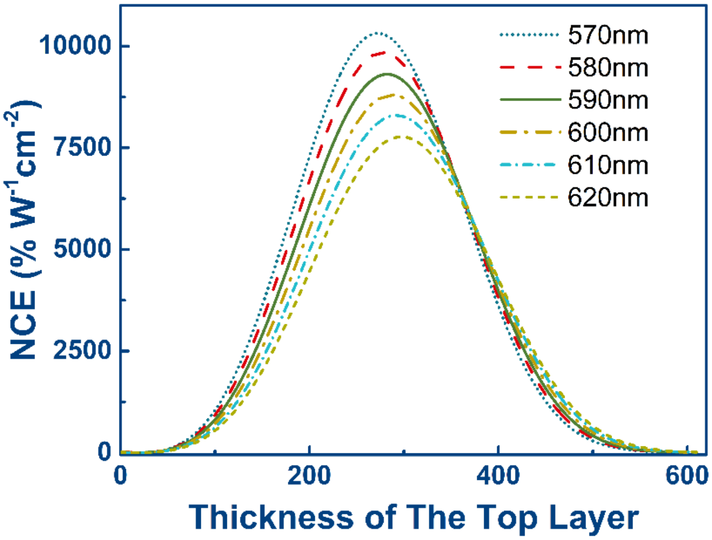

Fig. 10. The NCE values versus the relative thicknesses of LN layer. The top widths of the ridges are set to maintain the PM wavelength to be 1550 nm.

3.3. Thermal sensitivity

We have shown that the phase-matching condition is very sensitive to waveguide dimension variation, which places stringent requirements on the accuracy of the geometric parameters of the TFLN-based ridge waveguide. In the practical case, the thickness, top width, etching dept and sidewall angle of the ridge waveguides tends to deviate from the design values due to the fabrication errors. Therefore, it is critical to find a reliable tuning method to compensate these deviations. The extraordinary refractive index (n_e) of lithium niobate exhibits very large thermal-optic coefficient on the order of 10^{-5}, given by the following [40,41],

$$\frac{dn_{e,FW}}{dT} = -2.6 + 19.8 \times 10^{-3} T \tag{10}$$

$$\frac{dn_{e,SH}}{dT} = -2.6 + 22.4 \times 10^{-3} T \tag{11}$$

These equations are reliable in the temperature range of 300-515 K. We calculate the phase matching wavelength as a function of temperature ranges from 30 °C to 110 °C, showing in Fig. 11. We can see a nearly linear red shift trend between the phase matching wavelength and temperature in the figure. Linear fitting of each line in Fig. 11 reveals a temperature tuning sensitivity bigger than 0.11 nm/°C. This tuning ability is lower than the type I modal phase matching demonstrated in ref 29 because of the large difference of thermal-optic coefficients of ordinary/extraordinary refractive indices. We thought that the thermal isolated tuning setup could also be applied in the double-layered TFLN devices to realize a power-efficient thermal tuning SHG process [44].

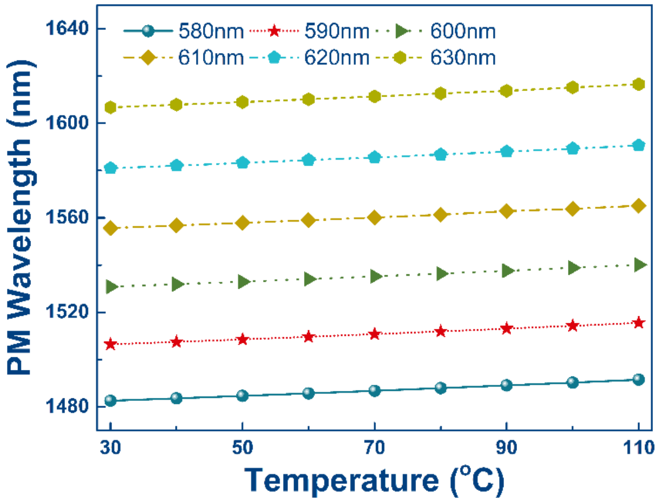

Fig. 11. The phase matching wavelength as a function of the temperature with different thicknesses of the ridge waveguides. The width of the ridge waveguides is set to be 1430 nm.

4. Summary

In this work, we investigated the MPM SHG process in ridge waveguide structure based on double-layered TFLN platform in the telecom C band. The phase matching wavelength versus the geometrical parameters (width, thickness, etching depth and sidewall angles) of ridge waveguides are investigated by the numerical simulations. The NCE of each phase matching points are also calculated and compared with the QPM scheme with the same geometric dimensions. Our findings show that MPM process in x-cut TFLN waveguides are very sensitive to the geometric dimensions of the ridge waveguides due to the mode dispersions in the higher mode regime. As a phase matching method with a strict constraint between phase matching wavelength and geometric dimensions, MPM is less versatile than QPM because the additional degree of freedom, $\chi^{(2)}$ grating, can be tuned in the latter case. However, the MPM process in double-layered TFLN ridge waveguides are very attractive as they offer the potential for efficient frequency conversion without the additional periodically electrical poling step.

Appendix

Table 1. A comparison of SHG ridge devices in TFLN working at telecom waveband. N/A: Cannot be inferred from the reported data.

Ref.	Type	NCE (%/W/cm^2)	FWHM (nm)	Length(mm)	dλ/dT (nm/K)	dλ/dW
[10]	QPM-TFLN	3757	1.0	5.0	0.1	-0.064
[14]	QPM-TFLN	2600	7.1[a]	4.0	N/A	-1.8[b]
[15]	QPM-TFLN	4600	14.0[c]	0.3	N/A	N/A
[21]	QPM-TFLN	2200	3.2[d]	4.0	N/A	N/A
[22]	QPM-Rib Loaded	160	3.0	4.8	N/A	N/A
[28]	QPM-Rib Loaded	1160	2.1	4.8	N/A	N/A
[33]	MPM-TFLN	41	3.0[e]	3.0	N/A	-0.66
[34]	MPM-TFLN	7.3	1.34[f]	8.0	0.84	N/A
[35]	MPM-TFLN	26	2.1[g]	1.0	N/A	N/A
[37]	MPM-TiO$_2$/LN	650	N/A	2.35	N/A	N/A
[39]	MPM-LN/LN	5540	3.0	1.2	0.137	N/A

[a] Estimated from Fig. 2 in ref 10.
[b] Estimated from Fig. 3(b) in ref 10.
[c] Estimated from Fig. 2(f) and Fig. 2(c) in ref 15.
[d] Estimated from Fig. 3(a) in ref 21.
[e] Estimated from Fig. 4(c) in ref 33.
[f] Estimated from Fig. 3(a) in ref 34.
[g] Estimated from Fig. 7 in ref 35.

Funding. National Natural Science Foundation of China (11874239); National Key Research and Development Program of China (2019YFA0705000).

Acknowledgements. This work was supported in part by the National Key Research and Development Project no. 2019YFA0705000 and the National Natural Science Foundation of China under Project no. 11874239.

Disclosures. The authors declare no conflicts of interest.

Data availability. Data underlying the results presented in this paper are not publicly available at this time but may be obtained from the authors upon reasonable request.

References

1. G. Poberaj, H. Hu, W. Sohler, and P. Günter, "Lithium niobate on insulator (LNOI) for micro-photonic devices," Laser Photonics Rev. **6**(4), 488–503 (2012).
2. Y. Jia, L. Wang, and F. Chen, "Ion-cut lithium niobate on insulator technology: Recent advances and perspectives," Appl. Phys. Rev. **8**(1), 011307 (2021).
3. Y. Jia, J. Wu, X. Sun, X. Yan, R. Xie, L. Wang, Y. Chen, and F. Chen, "Integrated Photonics Based on Rare-Earth Ion-Doped Thin-Film Lithium Niobate," Laser Photonics Rev. **16**(9), 2200059 (2022).
4. G. Chen, N. Li, J. D. Ng, H. L. Lin, Y. Zhou, Y. H. Fu, L. Y. T. Lee, Y. Yu, A.-Q. Liu, and A. J. Danner, "Advances in lithium niobate photonics development status and perspectives," Adv. Photonics **4**(03), 034003 (2022).
5. D. Zhu, L. Shao, M. Yu, R. Cheng, B. Desiatov, C. J. Xin, Y. Hu, J. Holzgrafe, S. Ghosh, A. Shams-Ansari, E. Puma, N. Sinclair, C. Reimer, M. Zhang, and M. Lončar, "Integrated photonics on thin-film lithium niobate," Adv. Opt. Photonics **13**(2), 242 (2021).
6. J. Lin, F. Bo, Y. Cheng, and J. Xu, "Advances in on-chip photonic devices based on lithium niobate on insulator," Photonics Res. **8**(12), 1910 (2020).

7. S. Li, L. Cai, Y. Wang, Y. Jiang, and H. Hu, "Waveguides consisting of single-crystal lithium niobate thin film and oxidized titanium stripe," Opt. Express **23**(19), 24212–24219 (2015).
8. L. Cai, Y. Wang, and H. Hu, "Low-loss waveguides in a single-crystal lithium niobate thin film," Opt. Lett. **40**(13), 3013–3016 (2015).
9. M. Rusing, P. O. Weigel, J. Zhao, and S. Mookherjea, "Toward 3D Integrated Photonics Including Lithium Niobate Thin Films: A Bridge Between Electronics, Radio Frequency, and Optical Technology," IEEE Nanotechnology Mag. **13**(4), 18–33 (2019).
10. J. Zhao, M. Rusing, U. A. Javid, J. Ling, M. Li, Q. Lin, and S. Mookherjea, "Shallow-etched thin-film lithium niobate waveguides for highly-efficient second-harmonic generation," Opt. Express **28**(13), 19669–19682 (2020).
11. M. He, M. Xu, Y. Ren, J. Jian, Z. Ruan, Y. Xu, S. Gao, S. Sun, X. Wen, L. Zhou, L. Liu, C. Guo, H. Chen, S. Yu, L. Liu, and X. Cai, "High-performance hybrid silicon and lithium niobate Mach–Zehnder modulators for 100 Gbit s^{-1} and beyond," Nat. Photonics **13**(5), 359–364 (2019).
12. C. Wang, M. Zhang, X. Chen, M. Bertrand, A. Shams-Ansari, S. Chandrasekhar, P. Winzer, and M. Loncar, "Integrated lithium niobate electro-optic modulators operating at CMOS-compatible voltages," Nature **562**(7725), 101–104 (2018).
13. M. Zhang, B. Buscaino, C. Wang, A. Shams-Ansari, C. Reimer, R. Zhu, J. M. Kahn, and M. Loncar, "Broadband electro-optic frequency comb generation in a lithium niobate microring resonator," Nature **568**(7752), 373–377 (2019).
14. C. Wang, C. Langrock, A. Marandi, M. Jankowski, M. Zhang, B. Desiatov, M. M. Fejer, and M. Lončar, "Ultrahigh-efficiency wavelength conversion in nanophotonic periodically poled lithium niobate waveguides," Optica **5**(11), 1438 (2018).
15. A. Rao, K. Abdelsalam, T. Sjaardema, A. Honardoost, G. F. Camacho-Gonzalez, and S. Fathpour, "Actively-monitored periodic-poling in thin-film lithium niobate photonic waveguides with ultrahigh nonlinear conversion efficiency of 4600%$W^{-1}cm^{-2}$," Opt. Express **27**(18), 25920–25930 (2019).
16. J. Y. Chen, C. Tang, M. Jin, Z. Li, Z. Ma, H. Fan, S. Kumar, Y. M. Sua, and Y. P. Huang, "Efficient Frequency Doubling with Active Stabilization on Chip," Laser Photonics Rev. **15**(11), 2100091 (2021).
17. U. A. Javid, J. Ling, J. Staffa, M. Li, Y. He, and Q. Lin, "Ultrabroadband Entangled Photons on a Nanophotonic Chip," Phys. Rev. Lett. **127**(18), 183601 (2021).
18. A. A. Sayem, Y. Wang, J. Lu, X. Liu, A. W. Bruch, and H. X. Tang, "Efficient and tunable blue light generation using lithium niobate nonlinear photonics," Appl. Phys. Lett. **119**(23), 231104 (2021).
19. J. Lin, N. Yao, Z. Hao, J. Zhang, W. Mao, M. Wang, W. Chu, R. Wu, Z. Fang, L. Qiao, W. Fang, F. Bo, and Y. Cheng, "Broadband Quasi-Phase-Matched Harmonic Generation in an On-Chip Monocrystalline Lithium Niobate Microdisk Resonator," Phys. Rev. Lett. **122**(17), 173903 (2019).
20. M. G. Vazimali and S. Fathpour, "Applications of thin-film lithium niobate in nonlinear integrated photonics," Adv. Photonics **4**(3), 034001 (2022).
21. J.-Y. Chen, Y. Meng Sua, Z.-H. Ma, C. Tang, Z. Li, and Y.-P. Huang, "Efficient parametric frequency conversion in lithium niobate nanophotonic chips," OSA Continuum **2**(10), 2914 (2019).
22. L. Chang, Y. Li, N. Volet, L. Wang, J. Peters, and J. E. Bowers, "Thin film wavelength converters for photonic integrated circuits," Optica **3**(5), 531 (2016).
23. X. Zhang, X. Liu, R. Ma, Z. Chen, Z. Yang, Y. Han, B. Wang, S. Yu, R. Wang, and X. Cai, "Heterogeneously integrated III-V-on-lithium niobate broadband light sources and photodetectors," Opt. Lett. **47**(17), 4564–4567 (2022).
24. B. Desiatov and M. Lončar, "Silicon photodetector for integrated lithium niobate photonics," Appl. Phys. Lett. **115**(12), 121108 (2019).
25. C. Op de Beeck, B. Haq, L. Elsinger, A. Gocalinska, E. Pelucchi, B. Corbett, G. Roelkens, and B. Kuyken, "Heterogeneous III-V on silicon nitride amplifiers and lasers via microtransfer printing," Optica **7**(5), 386 (2020).
26. C. Op de Beeck, F. M. Mayor, S. Cuyvers, S. Poelman, J. F. Herrmann, O. Atalar, T. P. McKenna, B. Haq, W. Jiang, J. D. Witmer, G. Roelkens, A. H. Safavi-Naeini, R. Van Laer, and B. Kuyken, "III/V-on-lithium niobate amplifiers and lasers," Optica **8**(10), 1288 (2021).
27. A. Shams-Ansari, D. Renaud, R. Cheng, L. Shao, L. He, D. Zhu, M. Yu, H. R. Grant, L. Johansson, M. Zhang, and M. Lončar, "Electrically pumped laser transmitter integrated on thin-film lithium niobate," Optica **9**(4), 408 (2022).
28. A. Boes, L. Chang, M. Knoerzer, T. G. Nguyen, J. D. Peters, J. E. Bowers, and A. Mitchell, "Improved second harmonic performance in periodically poled LNOI waveguides through engineering of lateral leakage," Opt. Express **27**(17), 23919–23928 (2019).
29. J.-Y. Chen, Z.-H. Ma, Y. M. Sua, Z. Li, C. Tang, and Y.-P. Huang, "Ultra-efficient frequency conversion in quasi-phase-matched lithium niobate microrings," Optica **6**(9), 1244 (2019).
30. J. Lu, J. B. Surya, X. Liu, A. W. Bruch, Z. Gong, Y. Xu, and H. X. Tang, "Periodically poled thin-film lithium niobate microring resonators with a second-harmonic generation efficiency of 250,000%/W," Optica **6**(12), 1455 (2019).
31. T. Matsushita, Y. Nakamura, and T. Kondo, "Design of zigzag folded inversion-stacked AlGaAs waveguides for ultra-compact wavelength converters," Opt. Express **25**(19), 22829–22839 (2017).
32. H. Ito and H. Inaba, "Efficient phase-matched second-harmonic generation method in four-layered optical-waveguide structure," Opt. Lett. **2**(6), 139–141 (1978).

33. C. Wang, X. Xiong, N. Andrade, V. Venkataraman, X. F. Ren, G. C. Guo, and M. Lončar, "Second harmonic generation in nano-structured thin-film lithium niobate waveguides," Opt. Express **25**(6), 6963–6973 (2017).
34. R. Luo, Y. He, H. Liang, M. Li, and Q. Lin, "Highly tunable efficient second-harmonic generation in a lithium niobate nanophotonic waveguide," Optica **5**(8), 1006 (2018).
35. J.-Y. Chen, Y. M. Sun, H. Fan, and Y.-P. Huang, "Modal phase matched lithium niobate nanocircuits for integrated nonlinear photonics," OSA Continuum **1**(1), 229 (2018).
36. L. Wang, L.-Q. Li, X.-T. Zhang, and F. Chen, "Type-I phase matching in thin film of lithium niobate on insulator," Results Phys. **16**, 103011 (2020).
37. R. Luo, Y. He, H. Liang, M. Li, and Q. Lin, "Semi-Nonlinear Nanophotonic Waveguides for Highly Efficient Second-Harmonic Generation," Laser Photonics Rev. **13**(3), 1800288 (2019).
38. X. Zhang, C. Sun, B. Xiong, Z. Hao, J. Wang, L. Wang, Y. Han, H. Li, and Y. Luo, "Antisymmetric-Nonlinear LNOI Waveguide for Highly Efficient Second-Harmonic Generation," *ACP* 2020 M4A.29 (2020).
39. L. Wang, X. Zhang, and F. Chen, "Efficient Second Harmonic Generation in a Reverse-Polarization Dual-Layer Crystalline Thin Film Nanophotonic Waveguide," Laser Photonics Rev. **15**(12), 2100409 (2021).
40. L. Moretti, M. Iodice, F. G. Della Corte, and I. Rendina, "Temperature dependence of the thermo-optic coefficient of lithium niobate, from 300 to 515 K in the visible and infrared regions," J. Appl. Phys. **98**(3), 036101 (2005).
41. D. E. Zelmon, D. L. Small, and D. Jundt, "Infrared corrected Sellmeier coefficients for congruently grown lithium niobate and 5 mol. % magnesium oxide–doped lithium niobate," J. Opt. Soc. Am. B **14**(12), 3319–3322 (1997).
42. D. Dai and M. Zhang, "Mode hybridization and conversion in silicon-on-insulator nanowires with angled sidewalls," Opt. Express **23**(25), 32452–32464 (2015).
43. A. Kaushalram, G. Hegde, and S. Talabattula, "Mode hybridization analysis in thin film lithium niobate strip multimode waveguides," Sci. Rep. **10**(1), 16692 (2020).
44. X. Liu, C. Zhang, Y. Pan, R. Ma, X. Zhang, M. Chen, L. Liu, Z. Xie, S. Zhu, S. Yu, and X. Cai, "Thermally tunable and efficient second-harmonic generation on thin-film lithium niobate with integrated micro-heater," Opt. Lett. **47**(19), 4921–4924 (2022).